International Journal of Solids and Structures 48 (2011) 1000–1010

Contents lists available at ScienceDirect

International Journal of Solids and Structures

journal homepage: www.elsevier.com/locate/ijsolstr

On crystal plasticity formability analysis for magnesium alloy sheets

H. Wang [a], P.D. Wu [a,*], K.P. Boyle [b], K.W. Neale [c]

[a] Department of Mechanical Engineering, McMaster University, Hamilton, Ontario, Canada L8S 4L7
[b] CANMET Materials Technology Laboratory, Ottawa, Ontario, Canada K1A 0G1
[c] Faculty of Engineering, University of Sherbrooke, Sherbrooke, Quebec, Canada J1K 2R1

ARTICLE INFO

Article history:
Received 11 July 2010
Received in revised form 25 October 2010
Available online 13 December 2010

Keywords:
Crystal plasticity
Magnesium
Formability
Texture
Strain path change

ABSTRACT

Sheet metal formability is assessed in terms of the Forming Limit Diagram (FLD) for magnesium alloys with Hexagonal Close Packed (HCP) crystallographic structure. All simulations are based on the recently developed elastic–visco-plastic self-consistent (EVPSC) model and the classical Taylor model, in conjunction with the M–K approach. The role of crystal plasticity models and the effects of basal texture on formability of magnesium alloy AZ31B sheet are studied numerically. It is observed that formability in HCP polycrystalline materials is very sensitive to the intensity of the basal texture. The path-dependency of formability is examined based on different non-proportional loading histories, which are combinations of two linear strain paths. It is found that while the FLD in strain space is very sensitive to strain path changes, the Forming Limit Stress Diagram (FLSD) in stress space is much less path-dependent. It is suggested that the FLSD is much more favourable than the FLD in representing forming limits in the numerical simulation of sheet metal forming processes. The numerical results are found to be in good qualitative agreement with experimental observations.

1. Introduction

The concept of the Forming Limit Diagram (FLD) has been used to represent conditions for the onset of sheet necking (see, e.g. Hecker, 1975); this is now a standard tool for characterizing materials in terms of their overall forming behavior. Most theoretical and numerical FLD analyses have been based on the so-called M–K approach, developed by Marciniak and Kuczynski (1967). Within the M–K framework, the influence of various constitutive features on FLDs has been explored using phenomenological plasticity models (see, e.g. Neale and Chater, 1980; Wu et al., 2003) and crystal plasticity (see, e.g. Zhou and Neale, 1995; Wu et al., 1997; Inal et al., 2005; Signorelli et al., 2009). Using the M–K approach, the predicted FLDs based on crystal plasticity were in good agreement with measured FLDs for rolled aluminum alloy sheets (Wu et al., 1998; Knockaert et al., 2002). However, almost all the FLD analyses have been for polycrystalline sheet metals with Face Centered Cubic (FCC) and Body Centered Cubic (BCC) crystallographic structures. Only very recently, Neil and Agnew (2009) and Lévesque et al. (2010) carried out crystal plasticity based FLD analyses for magnesium alloys with Hexagonal Close Packed (HCP) crystallographic structure, based on respectively the visco-plastic self-consistent (VPSC) model developed by Molinari et al. (1987) and Lebensohn and Tomé (1993) and the Taylor-type model proposed by Kalidindi (1998).

In the present paper, an FLD analysis for magnesium alloy AZ31B sheet is carried out based on the elastic–visco-plastic self-consistent (EVPSC) model recently developed by Wang et al. (2010c) and the classical Taylor model (Taylor, 1938), in conjunction with the M–K approach. The main purposes of this paper are to study (1) the effect of basal texture on formability; (2) the role of constitutive model on predicted FLDs; and (3) the path-dependency of formability. To the best of our knowledge, all these three important aspects have not been addressed for HCP polycrystalline sheets.

First of all, it is well-known that conventionally processed magnesium sheet exhibits very limited formability, due to the limited number of plastic deformation modes available. This can be explained based on the deformation behavior of magnesium single crystals deformed in uniaxial or biaxial tension with the basal plane parallel to the loading direction. In this case, the imposed extension is accompanied by contraction normal to the loading axis, in the direction tangential to the basal plane; very limited reduction normal to the basal plane is observed, and the crystals exhibit low ductility (Reed-Hill and Robertson, 1957). This behavior has strong implications for the room temperature formability of HCP magnesium wrought alloys, in which the basal planes typically lie preferentially in the plane normal to the primary compression direction imposed during processing. However, recent experimental works have revealed that formability of magnesium sheets can be significantly improved through texture optimization

* Corresponding author. Tel.: +1 905 525 9140x20092; fax: +1 905 572 7944.
E-mail address: peidong@mcmaster.ca (P.D. Wu).

0020-7683/$ - see front matter © 2010 Elsevier Ltd. All rights reserved.
doi:10.1016/j.ijsolstr.2010.12.004

by mainly re-orientating basal plane. For example, Huang et al. (2008) have reported an increase in the uniform strain prior to necking in AZ31 sheet produced by differential speed rolling (DSR), where the basal poles are tilted ~15° in the rolling direction (RD). Chino et al. (2008) have observed enhanced tensile ductility of AZ31 bar through torsional extrusion (TE), where the basal poles are inclined ~30° to the extrusion direction. Mukai et al. (2001) and Agnew et al. (2004) have shown that enhanced ductility can be achieved through equal channel angular extrusion (ECAE), where the basal planes are preferentially inclined ~45° to the extrusion direction. In a recently study, Wang et al. (2010b) investigated the influence of basal texture on the uniform strain under uniaxial tension and the limit strain under in-plane plane strain tension. This preliminary study suggested that formability can be significantly improved by controlling texture even without grain refinement. The present paper carries out a detailed study on the effects of basal texture on FLDs.

Secondly, it is also well-known that predicted FLDs are sensitive to the constitutive modes employed (see, e.g. Wu et al., 2003). Motivated by the works on effects of texture on formability of aluminum alloy sheets (Wu et al., 2004a; Kuroda and Ikawa, 2004; Yoshida et al., 2007). Signorelli and Bertinetti (2009) recently investigated how the cube texture affects the formability of FCC sheet metals. It was found that the predicted FLDs based on the VPSC model are quite different to the ones based on the classical Taylor model. In the present paper, the role of the constitutive model on formability of HCP sheet metals is assessed by comparing the predicted FLDs based on the EVPSC model with various self-consistent schemes and the classical Taylor model.

Finally, both experimental and numerical results have indicated that FLDs for FCC and BCC sheet metals are very sensitive to strain path changes (see, e.g. Kikuma and Nakajima, 1971; Laukonis and Ghosh, 1978; Graf and Hosford, 1994; Zhao et al., 1996; Hiwatashi et al., 1998; Kuroda and Tvergaard, 2000; Wu et al., 2000, 2005). Knowing the drawback of conventional FLDs, Arrieux et al. (1982), among others, represented formability based on the state of stress rather than the state of strain. They constructed a Forming Limit Stress Diagram (FLSD) by plotting the calculated principal stresses at necking. It was concluded that all FLSDs, based on phenomenological plasticity models such as Hill (1948) and Hosford (1979) and crystal plasticity theory (Asaro and Needleman, 1985), were almost path-independent (Arrieux, 1995; Zhao et al., 1996; Stoughton, 2000; Stoughton and Zhu, 2004; Wu et al., 2000, 2005). However, effects of strain path changes have not been studied for HCP polycrystalline sheets. This paper examines the path-dependency of the formability for HCP polycrystalline sheets. In these simulations, non-proportional loading histories are developed using combinations of two linear strain paths. The first strain path, the pre-strain operation, is common to all loading histories. Subsequent linear deformation paths are imposed by varying the strain-rate ratio for the development of an FLD applicable to that given pre-strain path and amount.

The paper is outlined as follows. In Section 2, the EVPSC model is briefly introduced. The problem is formulated in Section 3. Followed by the calibration of the models against experimental stress–strain curves, numerical results and discussions are provided in Section 4. Finally, Section 5 presents conclusions.

2. Constitutive model

The elastic–visco-plastic self-consistent (EVPSC) model for polycrystals recently developed by Wang et al. (2010c) is a completely general elastic–viscoplastic, fully anisotropic, self-consistent polycrystal model, applicable to large strains and to any crystal symmetry. Here, we very briefly describe the model. For details we refer to Wang et al. (2010c).

The elastic constitutive equation for a crystal is:

$$\overset{\nabla^*}{\boldsymbol{\sigma}} = \boldsymbol{L} : \boldsymbol{d}^e - \boldsymbol{\sigma} tr(\boldsymbol{d}^e), \tag{1}$$

where $\boldsymbol{L}$ is the fourth order elastic stiffness tensor, $\boldsymbol{d}^e$ is the elastic strain rate tensor and $\overset{\nabla^*}{\boldsymbol{\sigma}}$ is the Jaumann rate of the Cauchy stress $\boldsymbol{\sigma}$ based on the lattice spin tensor $\boldsymbol{w}^e$. The single crystal elastic anisotropy is included in $\boldsymbol{L}$ through the crystal elastic constants C_{ij} (Wang and Mora, 2008). If elasticity is assumed to be isotropic, $\boldsymbol{L}$ is a function only of Young's modulus, E, and Poisson's ratio, υ.

Plastic deformation of a crystal is assumed to be due to crystallographic slip and twinning on systems $(\boldsymbol{s}^\alpha, \boldsymbol{n}^\alpha)$. Here, $\boldsymbol{s}^\alpha$ and $\boldsymbol{n}^\alpha$ are the slip/twinning direction and the direction normal to the slip/twinning plane for system α, respectively. The following equation gives the grain (crystal) level plastic strain rate $\boldsymbol{d}^p$ (see, e.g. Asaro and Needleman, 1985):

$$\boldsymbol{d}^p = \dot{\gamma}_0 \sum_\alpha \boldsymbol{P}^\alpha \left| \frac{\tau^\alpha}{\tau^\alpha_{cr}} \right|^{\frac{1}{m}-1} \frac{\tau^\alpha}{\tau^\alpha_{cr}}, \tag{2}$$

where $\dot{\gamma}_0$ is a reference value for the slip/twinning rate, m is the slip/twinning rate sensitivity, $\boldsymbol{P}^\alpha = (\boldsymbol{s}^\alpha \boldsymbol{n}^\alpha + \boldsymbol{n}^\alpha \boldsymbol{s}^\alpha)/2$ is the Schmid tensor for system α, and $\tau^\alpha = \boldsymbol{\sigma} : \boldsymbol{P}^\alpha$ and τ^α_{cr} are the resolved shear stress (RSS) and critical resolved shear stress (CRSS) for system α, respectively. The evolution of τ^α_{cr} due to hardening processes is given by:

$$\dot{\tau}^\alpha_{cr} = \frac{\mathrm{d}\hat{\tau}^\alpha}{\mathrm{d}\gamma_{ac}} \sum_\beta h^{\alpha\beta} \dot{\gamma}^\beta, \tag{3}$$

where $\gamma_{ac} = \sum_\alpha |\gamma^\alpha|$ is the accumulated shear strain in the grain, and $h^{\alpha\beta}$ are the latent hardening coupling coefficients, which empirically account for the obstacles on system α associated with system β. $\hat{\tau}^\alpha$ is the threshold stress and is characterized by:

$$\hat{\tau}^\alpha = \tau^\alpha_0 + (\tau^\alpha_1 + h^\alpha_1 \gamma_{ac}) \left(1 - \exp\left(-\frac{h^\alpha_0}{\tau^\alpha_1} \gamma_{ac} \right) \right). \tag{4}$$

Here, τ_0, h_0, h_1 and $\tau_0 + \tau_1$ are the initial CRSS, the initial hardening rate, the asymptotic hardening rate, and the back-extrapolated CRSS, respectively. The polar nature of twinning is incorporated into the model simply by specifying a very large CRSS for the reverse direction.

Various homogenization methods have been developed to characterize the mechanical behavior of a polycrystalline aggregate from the responses of their single crystals. Among them, the most popular Taylor model assumes that the strains of each grain are equal to the imposed macroscopic strains, and the macroscopic stresses are the average of the stresses over all the grains. Another popular homogenizing method is the self-consistent approach: each grain is treated as an ellipsoidal inclusion embedded in a Homogeneous Effective Medium (HEM), which is an aggregate of all the grains. Interactions between each grain and the HEM are described using the Eshelby inclusion formalism (Eshelby, 1957). During each deformation step, the single crystal constitutive rule (which describes the grain-level response) and the self-consistency criteria are solved simultaneously. This ensures that the grain-level stresses and strain rates are consistent with the boundary conditions imposed on the HEM. The behavior of the inclusion (single crystal) and of the HEM can be linearized as follows (Wang et al., 2010c):

$$\boldsymbol{d} = \boldsymbol{M}^e : \dot{\boldsymbol{\sigma}} + \boldsymbol{M}^v : \boldsymbol{\sigma} + \boldsymbol{d}_0, \tag{5}$$

$$\boldsymbol{D} = \overline{\boldsymbol{M}}^e : \dot{\boldsymbol{\Sigma}} + \overline{\boldsymbol{M}}^v : \boldsymbol{\Sigma} + \boldsymbol{D}_0, \tag{6}$$

where $\boldsymbol{M}^e$, $\boldsymbol{M}^v$ and $\boldsymbol{d}_0$ are the elastic compliance, the visco-plastic compliance, and the back-extrapolated term for the grain, respectively. $\overline{\boldsymbol{M}}^e, \overline{\boldsymbol{M}}^v, \boldsymbol{D}, \boldsymbol{\Sigma}$ and $\boldsymbol{D}_0$ are the corresponding terms for the HEM. The grain-level stress and strain rates are related self-consistently to the corresponding values for the HEM as follows:

$$(\boldsymbol{d}-\boldsymbol{D}) = -\widetilde{\boldsymbol{M}}^{e} : (\dot{\boldsymbol{\sigma}}-\dot{\boldsymbol{\Sigma}}) - \widetilde{\boldsymbol{M}}^{v} : (\boldsymbol{\sigma}-\boldsymbol{\Sigma}), \tag{7}$$

where the interaction tensors $\widetilde{\boldsymbol{M}}^{e}$ and $\widetilde{\boldsymbol{M}}^{v}$ are given by:

$$\widetilde{\boldsymbol{M}}^{e} = (\boldsymbol{I}-\boldsymbol{S}^{e})^{-1} : \boldsymbol{S}^{e} : \overline{\boldsymbol{M}}^{e}, \quad \widetilde{\boldsymbol{M}}^{v} = (\boldsymbol{I}-\boldsymbol{S}^{v})^{-1} : \boldsymbol{S}^{v} : \overline{\boldsymbol{M}}^{v}. \tag{8}$$

Here, $\boldsymbol{S}^{e}$ and $\boldsymbol{S}^{v}$ are the elastic and visco-plastic Eshelby tensors for a given grain, respectively. $\boldsymbol{I}$ is the identity tensor.

Different self-consistent schemes (SCSs) depend on different choices for the linearization. Among various SCSs, the Secant SCS employs the following linearization:

$$\begin{aligned} M_{ijkl}^{v,secant} &= \dot{\gamma}_0 \sum_{\alpha} \left(\frac{\tau^{\alpha}}{\tau_{cr}^{\alpha}}\right)^{\frac{1}{m}-1} \frac{P_{ij}^{\alpha} P_{kl}^{\alpha}}{\tau_{cr}^{\alpha}}, \\ d_{0ij}^{secant} &= 0, \end{aligned} \tag{9}$$

while the Affine SCS applies the linearization:

$$\begin{aligned} M_{ijkl}^{v,affine} &= \frac{\dot{\gamma}_0}{m} \sum_{\alpha} \left(\frac{\tau^{\alpha}}{\tau_{cr}^{\alpha}}\right)^{\frac{1}{m}-1} \frac{P_{ij}^{\alpha} P_{kl}^{\alpha}}{\tau_{cr}^{\alpha}}, \\ d_{0ij}^{affine} &= \left(1-\frac{1}{m}\right) d_{ij}^{g}. \end{aligned} \tag{10}$$

With the aid of the Tangent and Secant relation: $\overline{\boldsymbol{M}}^{v,tangent} = \overline{\boldsymbol{M}}^{v,secant}/m$ (Hutchinson, 1976), the interaction tensor in the Tangent self-consistent scheme is given by:

$$\widetilde{\boldsymbol{M}}^{v} = \frac{1}{m}(\boldsymbol{I}-\boldsymbol{S}^{v})^{-1} : \boldsymbol{S}^{v} : \overline{\boldsymbol{M}}^{v,secant}. \tag{11}$$

Molinari and Tóth (1994) introduced a scalar interaction parameter m^{eff} by tuning the self consistent predictions with the finite element results. The resulted m^{eff} SCS provides an intermediate interaction tensor:

$$\widetilde{\boldsymbol{M}}^{v} = \frac{1}{m^{eff}}(\boldsymbol{I}-\boldsymbol{S}^{v})^{-1} : \boldsymbol{S}^{v} : \overline{\boldsymbol{M}}^{v,secant}. \tag{12}$$

The scheme would produce a rigid upper bound solution when $m^{eff} = \infty$. If $m^{eff} = m$ is assumed, this scheme reduces to the Tangent scheme (see also Tomé (1999)).

For details concerning the self-consistent equations associated with the different visco-plastic self-consistent algorithms, we refer the interested reader to Lebensohn et al. (2007).

Very recently, Wang et al. (2010a) evaluated several self-consistent approaches by studying the large strain behavior of magnesium alloy AZ31B sheet under different deformation processes. It was found that, of the approaches examined, the Affine self-consistent and m^{eff} self-consistent with interaction stiffness between the Secant (stiff) and Tangent (compliant) give the best results. Therefore, the EVPSC model with the Affine self-consistent scheme and m^{eff} self-consistent scheme, together with the classical Taylor model, are employed to study the role of constitutive model on FLDs.

To model the twinning activity, the Predominant Twin Reorientation (PTR) scheme proposed by Tomé et al. (1991) is used. PTR prevents grain reorientation by twinning until a threshold value A^{th1} is accumulated in any given system and rapidly raises the threshold to a value around $A^{th1} + A^{th2}$.

For simplicity, EVPSC models with the Affine and m^{eff} SCSs are respectively called the Affine and meff models in the rest of the present paper.

3. Problem formulation and method of solution

Following the numerical procedure developed by Wu et al. (1997), the EVPSC model outlined above, in conjunction with the M–K approach, is implemented into a numerical code for constructing the FLDs. We assume that the axes x_1 and x_2 define the rolling direction (RD) and the transverse direction (TD) in the plane of the sheet, while x_3 represents the direction normal to the sheet (ND). The basic assumption of the M–K approach is the existence of material imperfections in the form of grooves that is initially inclined at an angle ψ_I with respect to the x_1 reference direction (Fig. 1). Marciniak and Kuczynski (1967) showed that a slight intrinsic inhomogeneity in load bearing capacity throughout a deforming sheet can lead to unstable growth of strain in the region of the imperfection, and subsequently cause localized necking and failure. In the present paper, quantities inside the groove are denoted by $(\ )^b$. The thickness along the minimum section in the groove is denoted by $h^b(t)$, with an initial value $h^b(0)$. The initial geometric non-uniformity is defined by

$$f_0 = \frac{h^b(0)}{h(0)} \tag{13}$$

with $h(0)$ being the initial sheet thickness outside the imperfection groove.

The deformation outside the imperfection groove is assumed to be:

$$\frac{D_{22}}{D_{11}} = \frac{\dot{\varepsilon}_{22}}{\dot{\varepsilon}_{11}} = \rho, \quad D_{12} = 0, \quad W_{12} = 0, \tag{14}$$

where $\dot{\varepsilon}_{11} = D_{11}$ and $\dot{\varepsilon}_{22} = D_{22}$ are the (principal) logarithmic strain rates and the W_{ij} values are components of the spin tensor. It is further assumed that $D_{13} = D_{23} = W_{13} = W_{23} = 0$, while D_{33} is specified by the condition $\dot{\sigma}_{33} = 0$.

Under the imposed deformations described in (14), the evolution of the groove orientation ψ is given by

$$\dot{\psi} = n_1 n_2 (D_{11} - D_{22}) - (n_1^2 - n_2^2) D_{12}, \tag{15}$$

where $n_1 = \cos\psi$ and $n_2 = \sin\psi$ are the components of the unit normal to the band (Fig. 1). Here and subsequently, all quantities are in the current configuration.

Equilibrium and compatibility inside and outside the groove are automatically satisfied because uniform deformations are assumed both inside and outside the groove. The compatibility condition at the groove interface is given in terms of the differences in the velocity gradients inside and outside the groove:

$$L_{\xi\eta}^{b} = L_{\xi\eta} + v_{\xi} n_{\eta} \tag{16}$$

or

$$\begin{aligned} D_{\xi\eta}^{b} &= D_{\xi\eta} + \frac{1}{2}(v_{\xi} n_{\eta} + v_{\eta} n_{\xi}), \\ W_{\xi\eta}^{b} &= W_{\xi\eta} + \frac{1}{2}(v_{\xi} n_{\eta} - v_{\eta} n_{\xi}), \end{aligned} \tag{17}$$

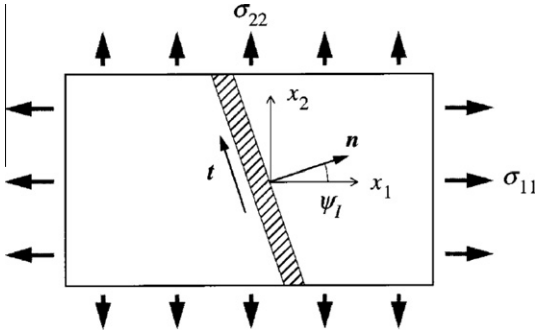

Fig. 1. The geometry and convention employed in the FLD analysis.

where v_ξ are parameters to be determined. Here, and subsequently, Greek indices range from 1 to 2. Equilibrium balance on each side of the interface requires that

$$n_\xi \sigma^b_{\xi\eta} h^b = n_\xi \sigma_{\xi\eta} h \tag{18}$$

in the current configuration. A set of incremental equations for v_ξ is now obtained by substituting the incremental constitutive Eq. (1) into the incremental form of (18), using (17) to eliminate the strain increments $D^b_{\xi\eta}$. Together with the condition $\dot{\sigma}^b_{33} = 0$, this furnishes three algebraic equations for solving v_1, v_2 and the unknown D^b_{33}. The sheet thickness outside the band h and inside the band h^b are updated based on the relations

$$\dot{h} = D_{33} h, \qquad \dot{h}^b = D^b_{33} h^b \tag{19}$$

The onset of sheet necking is defined by the occurrence of a much higher maximum principal logarithmic strain rate inside the band than outside, taken here as the condition $\dot{\varepsilon}^b / D_{11} \geqslant 10^5$, where $\dot{\varepsilon}^b$ represents the maximum strain rate inside the band. The corresponding principal logarithmic strains ε^*_{11} and ε^*_{22}, and principal stresses σ^*_{11} and σ^*_{22} outside the band are the limit strains and limit stresses, respectively. For a real sheet, numerous initial imperfections can exist with different orientations. A conservative estimate of the forming limit strain is that obtained from limit strain values for various values of the initial band orientation ψ_I, and then selecting the minimum value as the actual forming limit strain. The entire FLD of a sheet is determined by repeating the procedure for different strain paths outside the band as prescribed by the strain-rate ratio ρ. To study path-dependency of FLDs, non-proportional loading histories are developed using combinations of two linear strain paths. The first strain path; i.e. the pre-strain operation, is common to all loading histories. Subsequent linear deformation paths are imposed by varying the strain-rate ratio for the development of an FLD applicable to that given pre-strain path and amount.

4. Results and discussions

We assume that plastic deformation is due to slip in the Basal $\langle a\rangle$ $(\{0001\}\langle 11\bar{2}0\rangle)$, Prismatic $\langle a\rangle$ $(\{10\bar{1}0\}\langle 11\bar{2}0\rangle)$ and Pyramidal $\langle c+a\rangle$ $(\{\bar{1}\bar{1}22\}\langle\bar{1}\bar{1}23\rangle)$ slip systems, and twinning on the $\{10\bar{1}2\}\langle\bar{1}011\rangle$ tensile twin system (see Fig. 2). It is noted that Pyramidal $\langle a\rangle$ $(\{1\bar{1}01\}\langle 11\bar{2}0\rangle)$ slip system is frequently referred to in the magnesium literature. However, it has been reported that the Prismatic $\langle a\rangle$ slip is more important than Pyramidal $\langle a\rangle$ slip (Ward Flynn et al., 1961). Furthermore, as pointed out by Agnew et al. (2001), the kinds of deformations and crystallographic textures induced by Pyramidal $\langle a\rangle$ slip could also result from a combination of Basal $\langle a\rangle$ slip and Prismatic$\langle a\rangle$ slip. Therefore, Pyramidal $\langle a\rangle$ is not included in the present paper.

The elastic stiffness tensor $\boldsymbol{L}$ is a fourth order tensor. Due to its symmetric properties $L_{ijkl} = L_{jikl} = L_{ijlk}$, the elasticity tensor can be presented in terms of the following 6×6 matrix:

$$\boldsymbol{L} = \begin{bmatrix} L_{1111} & L_{1122} & L_{1133} & L_{1112} & L_{1113} & L_{1123} \\ & L_{2222} & L_{2233} & L_{2212} & L_{2213} & L_{2223} \\ & & L_{3333} & L_{3312} & L_{3313} & L_{3323} \\ & & & L_{1212} & L_{1213} & L_{1223} \\ & & & & L_{1313} & L_{1323} \\ \text{sym} & & & & & L_{2323} \end{bmatrix} \tag{20}$$

The elastic anisotropy of single crystals can be included by using the crystal elastic constants C_{ij} (Wang and Mora, 2008). For HCP materials,

$$\begin{aligned} &L_{1111} = L_{2222} = C_{11}, \quad L_{3333} = C_{33}, \\ &L_{1122} = C_{12}, \quad L_{1133} = C_{13}, \\ &L_{1212} = C_{66}, \quad L_{1313} = L_{2323} = C_{44} \end{aligned} \tag{21}$$

with the other components being zero. For an isotropic material one would have

$$\begin{aligned} &L_{1111} = L_{2222} = L_{3333} = \lambda + 2\mu, \\ &L_{1122} = L_{1133} = L_{2233} = \lambda, \\ &L_{1212} = L_{1313} = L_{2323} = \mu, \end{aligned} \tag{22}$$

where $\lambda = \frac{E\upsilon}{(1+\upsilon)(1-2\upsilon)}$ and $\mu = \frac{E}{2(1+\upsilon)}$ are the Lamè constants in terms of the Young's modulus E and the Poisson's ratio υ.

The reference material studied in the present paper is a magnesium alloy AZ31B sheet at room temperature. The experimentally measured mechanical behavior of the sheet has been reported by Jain and Agnew (2007). The measured {00.1} and {10.0} pole figures for the as-received reference sheet are shown in Fig. 3. This is a typical rolling texture with major and minor peaks close to ND, at about 5° and −5° along the RD, respectively. Fig. 3 also shows the pole figures obtained by rotating the reference texture by an angle α about TD. In the {00.1} pole figures, this rotation results in a vertical downward translation of the peaks in the reference texture (i.e. a downward translation of the peaks along RD). The intensity of the basal texture as a function of tilted angle α is shown in Fig. 4. The intensity is calculated as the ratio of the number of grains with a maximum orientation difference to the ideal basal orientation of less than 15°, to the total number of grains. The ideal basal grain corresponds to perfect alignment of the basal pole with the normal direction. It is interesting to note that the calculated intensity for $\alpha = 5°$ is higher than for $\alpha = 0°$ (reference texture). The reason for this is that the reference texture has its major peak at around 5° with respect to the RD. For $\alpha = 5°$, this peak is translated into the centre of the pole figure (i.e., the ideal orientation), resulting in the observed intensification of the basal texture. Nevertheless, the intensity decreases rapidly when the tilt angle is relatively large.

It is very important to be noted that the decrease in the intensity does not imply any weakening of the texture. It only represents that the rotation changes the orientation of dominant texture components with respect to the principal straining directions. Even thought the intensity parallel to the new sheet normal direction is lower, the overall texture is not weakened. It is also important to be pointed out that the equal channel angular extrusion, torsion extrusion, and differential speed rolling not only rotate the basal pole but also weaken the texture. In the present paper, while effects of the basal pole rotation on FLDs will be studied, influences of the texture weakening on FLDs will not be considered.

The reference slip/twinning rate, $\dot{\gamma}_0$, and the rate sensitivity, m, assumed to be same for all slip/twinning systems, are take as 0.001 s^{-1} and 0.05, respectively, unless otherwise mentioned. We further assume that elasticity is isotropic with Young's modulus $E = 2 \times 10^5$ MPa and Poisson's ratio $\upsilon = 0.33$. It is worth mentioning that $E = 0.45 \times 10^5$ MPa is frequently referred to in the magnesium literature. Wang et al. (2010c) have shown that the predicted stress–strain curves and texture evolution based on the EVPSC are not sensitive to the value of Young's modulus and are very close to those based on the VPSC models at large strains for monotonic loading. For example, the calculated stress–strain curves under monotonic loadings are not significantly dependent on the value of Young's modulus and are almost the same as the ones according to the VPSC model at large strains. Furthermore, with the value of the Young's modulus used, $E = 2 \times 10^5$ MPa, responses of the sheets considered are expected to be nearly rigid plastic, and the predictions based on the EVPSC model should be almost the same as those based on the VPSC model, even at small strains. The effect of Young's

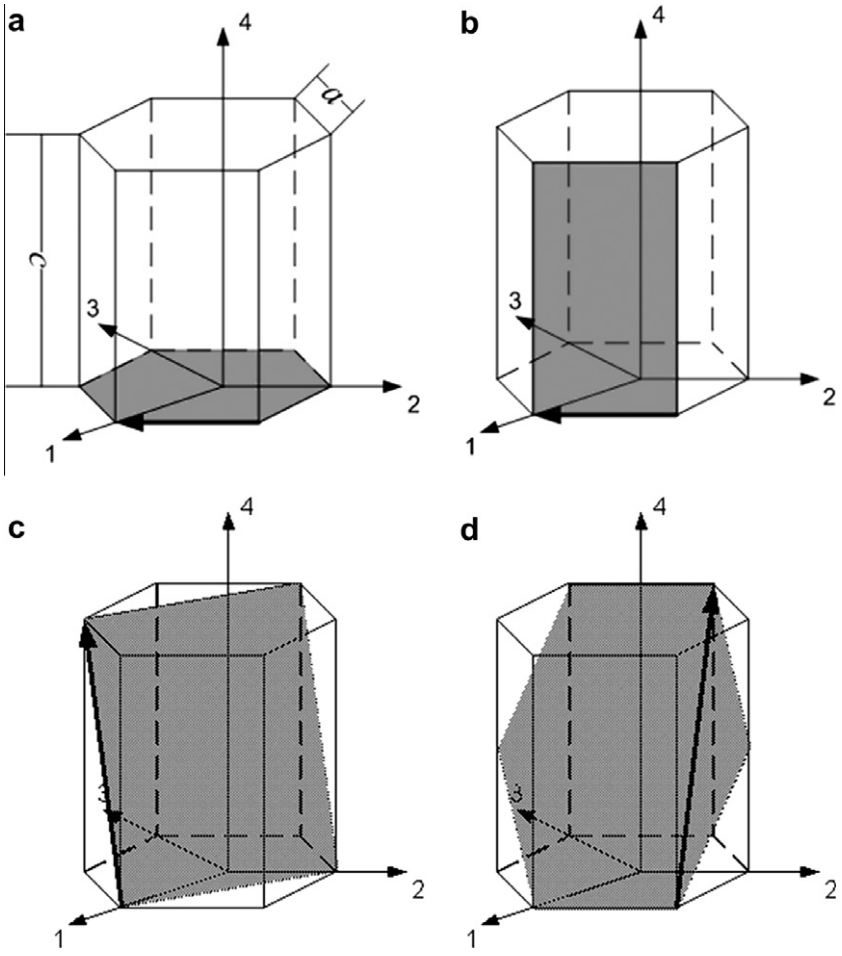

Fig. 2. Plastic deformation modes in hexagonal structure: (a) basal $\langle a \rangle$ slip systems, (b) prismatic $\langle a \rangle$ slip systems, (c) pyramidal $\langle c+a \rangle$ slip systems, and (d) tensile twin.

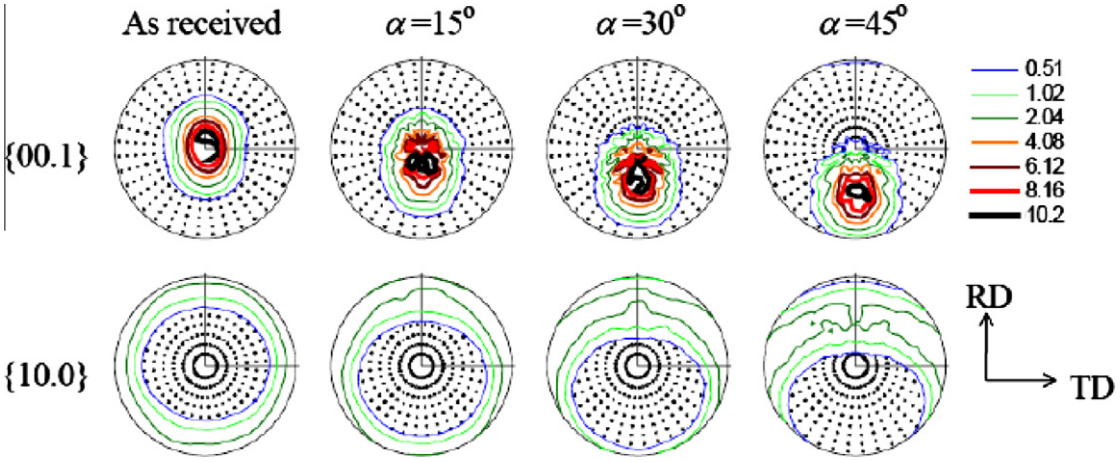

Fig. 3. Initial textures represented in terms of the {00.1} and {10.0} pole figures (from Wang et al. (2010b)).

modulus on the predicted limit strains was examined for the as-received sheet under in-plane plane strain tension. It was found that the choice of modulus did not affect the predict FLD value by more than 0.5%. Thus, without losing generality, using a very high value of Young's modulus makes it easy for us to validate the EVPSC model based FLD code because the difference in predictions between the EVPSC and VPSC is expected to be very small during the entire deformation process. However, the deformation process may involve unloading during strain path changes (Wu et al., 2005). Therefore, EVPSC model is preferential to simulate strain path changes because VPSC model cannot account for unloading.

Values of the other material parameters are estimated by fitting numerical simulations of uniaxial tension and compression along the RD to the corresponding experimental data for the reference sheet. In these simulations, a strain rate of $D_{11} = 0.001\ s^{-1}$ is prescribed in the loading direction, the only non-zero stress component is the normal stress along the loading direction. All of the strains are allowed to develop freely. Thus, in addition to the nor-

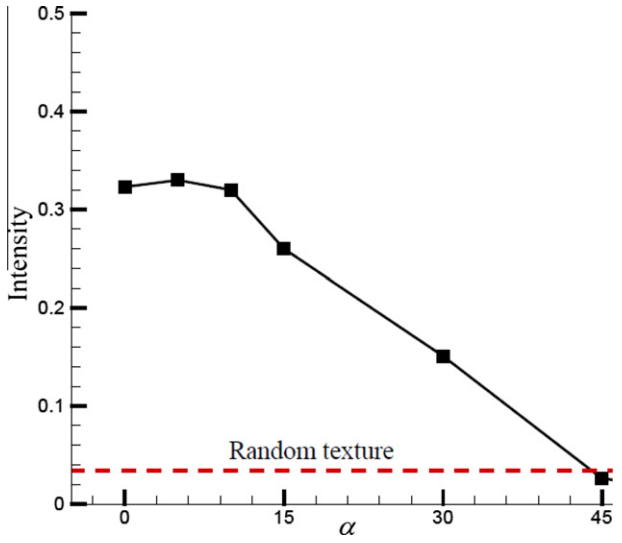

Fig. 4. The intensity of basal texture as a function of the tilted angle α (from Wang et al. (2010b)).

mal strains in the width and thickness directions, three shear strains are allowed to develop. Since the *c*-axes of the constituent grains are preferentially oriented normal to RD in the reference texture, tensile twinning contributes little to plastic deformation in uniaxial tension along the RD, but is the predominant plastic deformation mode in uniaxial compression at small strains. Thus, values for the material parameters associated with slip systems are determined from uniaxial tension along the RD, while values for the material parameters associated with twinning are determined from uniaxial compression along the RD. Fig. 5 presents the uniaxial tension and compression true stress and plastic strain curves along the RD. The importance of twinning in compression is clearly revealed by the characteristic S-shape of the flow curve. The Taylor model and EVPSC model associated with Affine self-consistent scheme and m-effective scheme fit the experimental stress strain curves well. Table 1 contains the material parameters obtained from the simulations. These parameters are used in all subsequent simulations.

We proceed by constructing FLDs using the value of the material parameters determined above. In all the simulations reported in the present paper, the initial geometric non-uniformity is taken

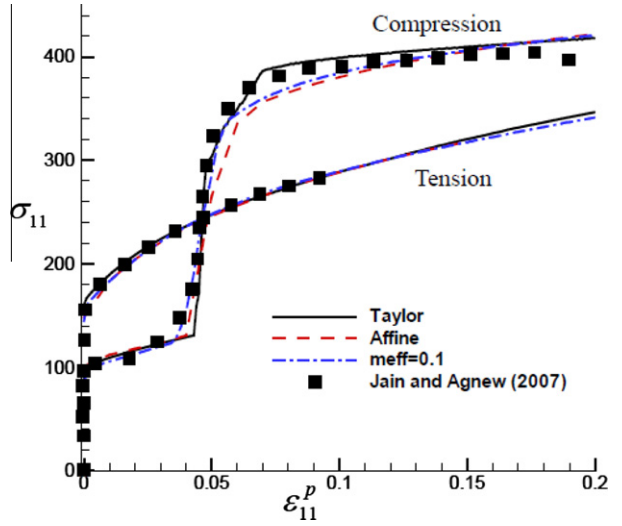

Fig. 5. True stress and plastic strain curves under uniaxial tension/compression along the RD. The experimental data are taken from Jain and Agnew (2007).

as $f_0 = 0.99$. It is noted that the value of f_0 is usually determined by fitting the measured limit strain at in-plane plane strain tension (Wu et al., 1998). Unfortunately, there are no available FLDs measured at room temperature for AZ31B. Fig. 6 shows the predicted FLDs for the reference sheet based on the Taylor, Affine and meff models. Generally speaking, all the models predict similar overall FLDs, which are analogical to the one obtained by Neil and Agnew (2009) at room temperature. It is seen from Fig. 6 that the predicted major limit strain ε_{11}^{*} decreases with ρ to reach its lowest point at $\rho \approx 0.1$ for all the models, and then increases until $\rho = 0.4$, 0.2 and 0.3 for the Taylor, Affine and meff models, respectively. With further increasing $\rho, \varepsilon_{11}^{*}$ once again decreases. It is interesting to note that the "hump" shown in Fig. 6 in the right-hand side of the predicted FLDs was also found by Chino et al. (2007) from the measured FLDs for magnesium alloy AZ31 sheet at elevated temperature. As mentioned previously, in the simulations we have scanned every 5° of a range of ψ_I and then determined the critical groove angle that gives the minimum localization strain, i.e. the limit strain. Fig. 7 gives the predicted critical groove orientations. It is seen that, for all the models employed, a groove oriented at $\psi_I = 0$ is favourable for necking when $-0.4 \leqslant \rho \leqslant 0.8$, while the critical groove orientation $\psi_I = 5°$ is found under uniaxial tension ($\rho = -0.5$). At equi-biaxial tension ($\rho = 1$) the critical groove orientations $\psi_I = 10°$, 20°, 10° are calculated based on the Taylor, Affine and meff models, respectively. When $\rho = 0.9$, the critical groove orientation $\psi_I = 10°$ is found for the meff model, while a groove oriented at $\psi_I = 0$ is favourable for the Taylor and Affine models.

Previous studies have indicated that FLDs are usually sensitive to the material rate sensitivity (e.g. Hutchinson and Neale, 1977; Wu et al., 1997). Fig. 8 shows the change in the predicted FLD based on the Affine model when the value of the material rate sensitivity m is decreased from 0.05 to 0.02. Decreasing the rate sensitivity tends to degrade the hardening at large strains. Consistent with this, Fig. 8 shows that the limit strain is decreased relative to that in Fig. 6. The effect of m on FLDs shown in Fig. 8 is similar to that based on the M–K approach in conjunction with phenomenological plasticity (Neale and Chater, 1980) and crystal plasticity for FCC polycrystals (Wu et al., 1997).

It is generally accepted that texture evolution has a significant effect on the initiation and propagation of shear bands in FCC polycrystalline metals (see, e.g. Inal et al., 2002a,b). In this paper, repeating calculations reported in Fig. 6 but turning off the texture evolution assesses the influence of the texture evolution on FLDs. Numerical results based on the Affine model are presented in Fig. 9. It is observed that texture evolution has a negligible effect on limit strains for strain paths nearby in-plane plane strain tension. However, texture evolution decreases the limit strains significantly when $\rho \geqslant 0.4$ or $\rho \leqslant -0.3$. The predicted effect of texture evolution shown in Fig. 9 is opposite to those found for FCC and BCC polycrystals. Wu et al. (2004b), 2007 have reported that texture evolution significantly increases the limit strains for strain paths $\rho \geqslant 0$ for FCC polycrystals, while Inal et al. (2005) have found that texture evolution has a negligible influence on predicted FLDs for BCC polycrystals.

The effects of initial texture on predicted FLDs have been extensively studied for FCC and BCC polycrystalline sheets (see, e.g. Wu et al., 1997, 1998). Figs. 10–12 present the influence of initial texture on the predicted FLDs based on the Taylor model, Affine model and meff model, respectively. All the models predict a general trend: formability of HCP sheets can be improved through rotating the reference texture by an angle α about the TD. It is noted that when $\alpha = 45°$ the intensity of basal texture is almost the same as that in a random texture (see Fig. 4), and consequently the predicted limit strains are comparable to those for random texture. Fig. 13 shows the predicted critical groove orientations when $\alpha =$

Table 1
List of values of material constants for various polycrystal plasticity models.

Model	Mode	τ_0	τ_1	h_0	h_1	Latent	A^{th1}	A^{th2}
Taylor	Basal	13	4	5000	30	4		
	Prismatic	73	35	400	60	4		
	Pyramidal	110	83	2500	0	2		
	Tensile twin	31	0	0	0	4	0.82	0
Affine	Basal	9	1	5000	25	4		
	Prismatic	79	40	590	50	4		
	Pyramidal	100	100	5000	0	2		
	Tensile twin	47	0	0	0	4	0.72	0
meff (m^{eff} = 0.1)	Basal	17	6	3800	100	4		
	Prismatic	77	33	650	50	4		
	Pyramidal	148	35	9600	0	2		
	Tensile twin	33	0	0	0	4	0.81	0

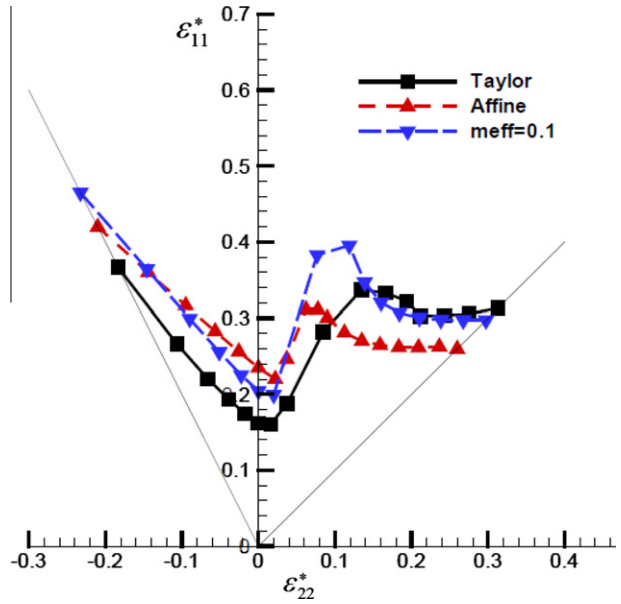

Fig. 6. Predicted FLDs for the reference sheet based on various polycrystal plasticity models.

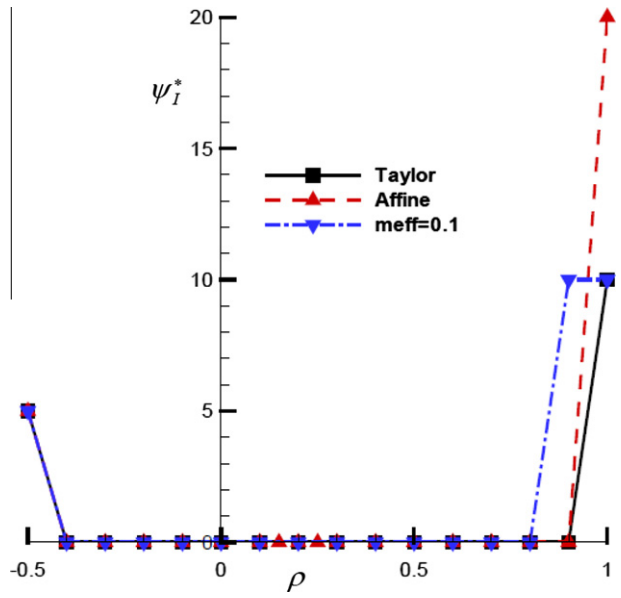

Fig. 7. Predicted critical groove orientations for the reference sheet based on various polycrystal plasticity models.

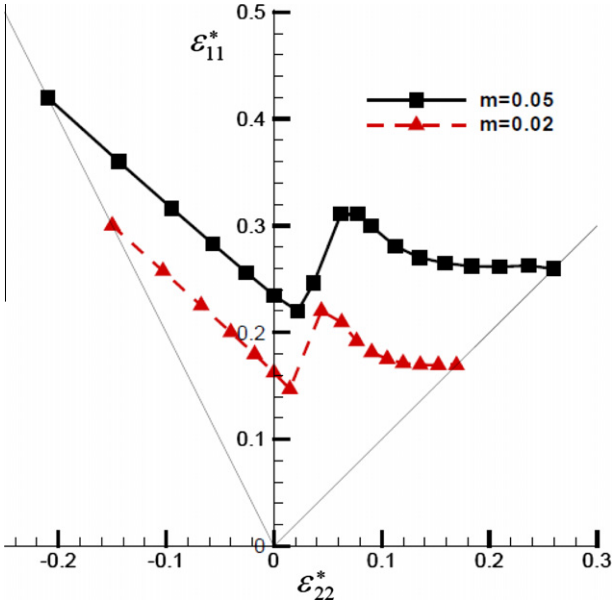

Fig. 8. Influence of the material rate sensitivity parameter m on the predicted FLDs for the reference sheet based on the Affine model.

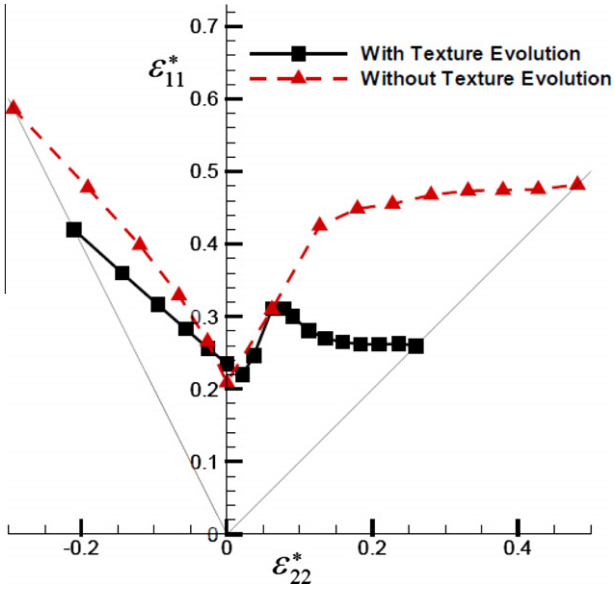

Fig. 9. Influence of texture evolution on the predicted FLDs for the reference sheet based on the Affine model.

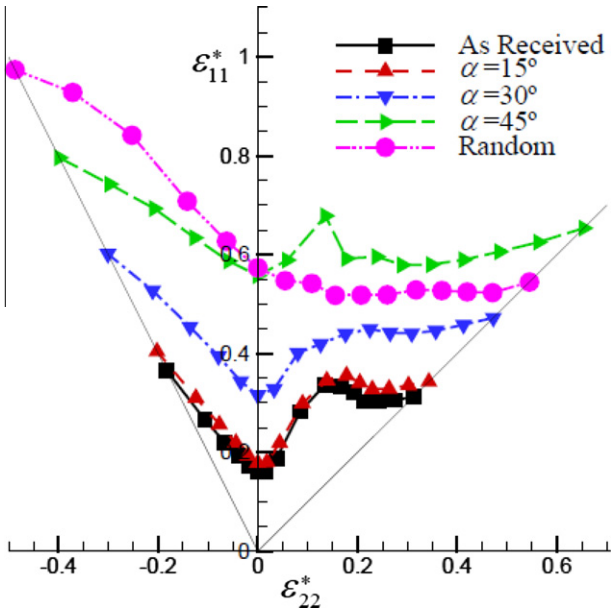

Fig. 10. Influence of initial texture on the predicted FLDs based on the Taylor model.

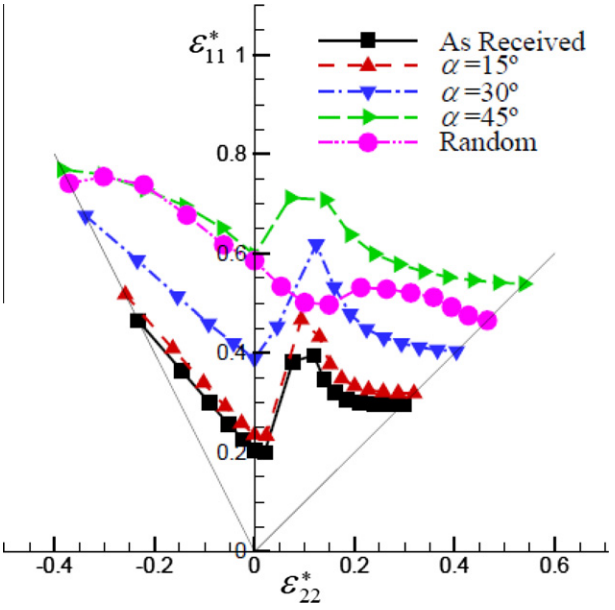

Fig. 12. Influence of initial texture on the predicted FLDs based on the meff model.

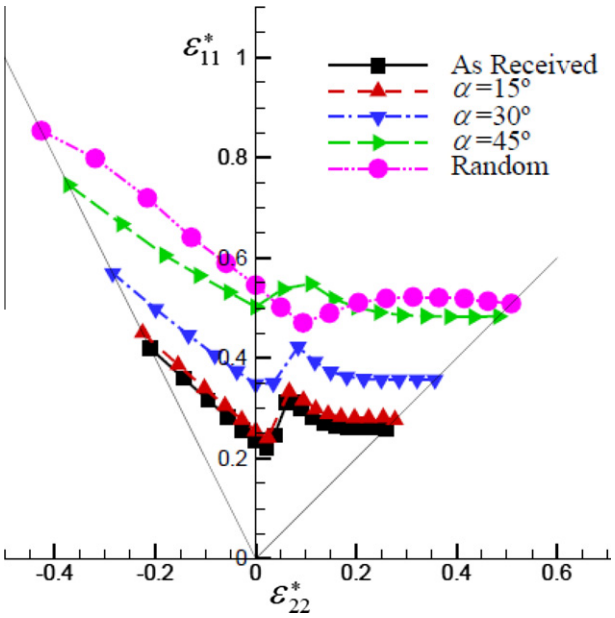

Fig. 11. Influence of initial texture on the predicted FLDs based on the Affine model.

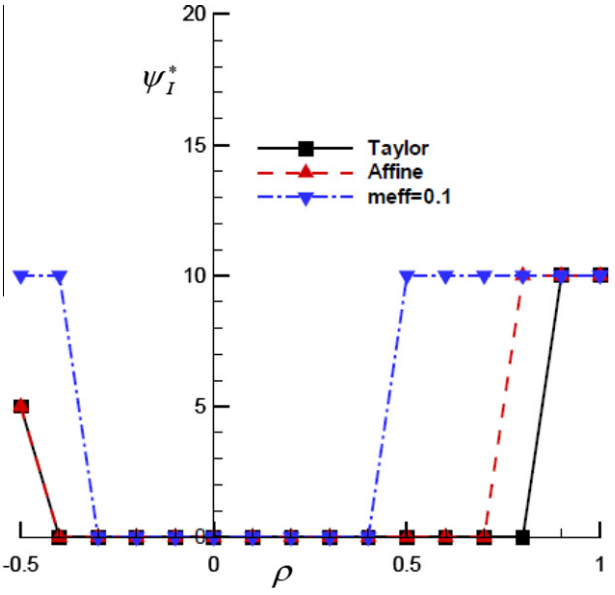

Fig. 13. Predicted critical groove orientations for the initial texture rotated 45° around TD based on various polycrystal plasticity models.

45°. It is seen that a groove oriented at $\psi_I = 0$ is favourable for necking when $-0.3 \leqslant \rho \leqslant 0.4$, for all models employed. Based on the Taylor model, the critical groove orientations ψ_I = 0°, 5° and 10° are found for $\rho = -0.4$, $\rho = -0.5$ and $\rho \geqslant 0.9$, respectively. According to the meff model, $\psi_I = 10°$ is the critical groove orientation for strain paths $\rho \geqslant 0.5$ or $\rho \leqslant -0.4$. The critical groove orientations $\psi_I = 5°$ and 10° are found respectively for $\rho = -0.5$ and $\rho \geqslant 0.8$ if the Affine model is applied. The effect of basal texture on formability is even more clearly exhibited in Fig. 14, which shows the predicted limit strain versus the tilted angle α under in-plane plane strain tension ($\rho = 0$) based on various models. It is clear that the predicted necking strain is dramatically increased when the tilted angles $\alpha > 15°$.

It is important to be noted that all the simulations reported above are assumed that the major straining direction is parallel to the RD. Fig. 15 shows the predicted major limit strains under uniaxial tension, in-plane plane strain tension and equi-biaxial tension when the major straining direction is parallel to the TD. Here, the major limit strains are normalized by the corresponding limit strains for the as-received sheet (i.e. $\alpha = 0$). To avoid congestion, the origin is shifted by 0.5 parallel to ordinate in Fig. 15. Obviously, the predicted formability under equi-biaxial tension ($\rho = 1$) is same as the one in the case of the major straining direction being parallel to the RD. Under uniaxial tension ($\rho = -0.5$), the predicted major limit strain is independent of the titled angle α. The reason for this is that the rotation of the texture is around the TD and thus the rotation does not affect the uniaxial tension along the TD (Wang et al., 2010b). Under in-plane plane strain tension ($\rho = 0$), the formability is less dramatically improved by rotating the texture around the TD if the major straining direction is parallel to

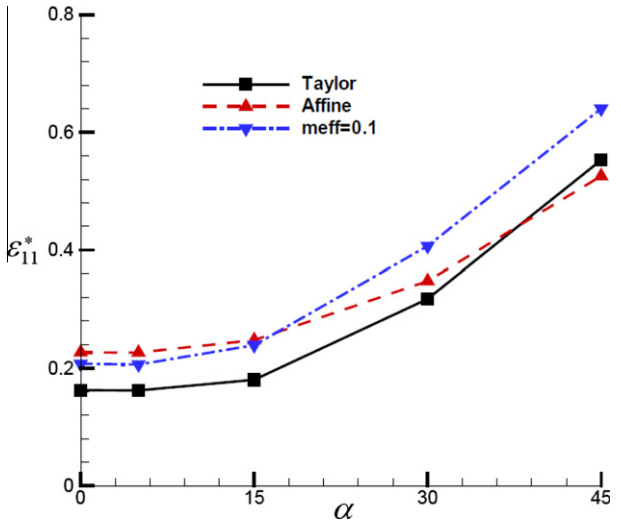

Fig. 14. Influence of basal texture on the predicted limit strain under in-plane plane strain tension ($\rho = 0$).

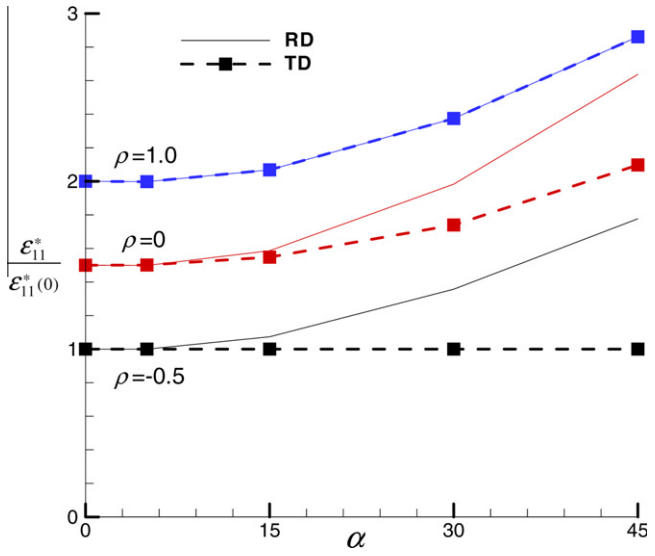

Fig. 15. Predicted major limit strains when the major straining direction is parallel to the TD. The origin is shifted by 0.5 parallel to ordinate so as to avoid congestion.

the TD. These results are in good agreement with the experimental observation made by Agnew et al. (2004).

Figs. 10–14, together with Figs. 6 and 7, clearly indicate that if values of material parameters in the constitutive models are determined by best-fitting the same experimental data, the constitutive models predict similar FLDs. In other words, the difference in the predicted FLDs between various models is quantitative rather than qualitative.

Finally, the effects of strain path changes on FLDs for the reference sheet are numerically studied based on the Affine model. The sheet is pre-strained respectively in uniaxial tension ($\rho = -0.5$), in-plane plane strain tension ($\rho = 0$) and equi-biaxial tension ($\rho = 1$). When the designed pre-strain level is reached, the current imperfection f and deformation state inside and outside the groove are used as the starting state for the subsequent strain path in the FLD analysis.

Fig. 16 shows FLDs for both the as-received and sheets pre-strained in uniaxial stretching up to $\varepsilon_{11} = 0.1$ and 0.15, respectively. It is clear that uniaxial pre-straining not only shifts the whole FLDs

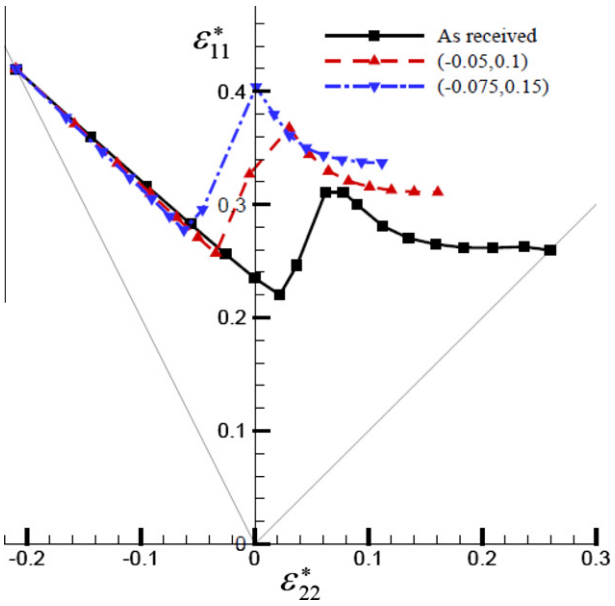

Fig. 16. Predicted FLDs for the reference sheet pre-strained to different levels in uniaxial tension ($\rho = -0.5$) based on the Affine model.

to the left, but also shifts the FLDs upwards. The use of uniaxial tension pre-strain can thus lead to large regions of strain path enhanced formability, where strain states can be reached through non-proportional histories which could not be achieved by proportional histories. Fig. 17 shows the predicted FLDs following in-plane plane strain tension operations. As expected, the limit strain for in-plane plane strain tension is not affected by the pre-straining. The FLD shape exhibits a trend of changing from U towards V due to the pre-straining. More specifically, for strain paths $\rho \geqslant 0.3$, it is found that the pre-straining has almost no effect on the limit strain ε_{11}, but it dramatically decreases the limit strain ε_{22}. For subsequent strain paths $\rho < 0$, the pre-straining reduces both limit strains ε_{11} and ε_{22}. The FLD predicted following equi-biaxial pre-straining is shown in Fig. 18. The formability associated

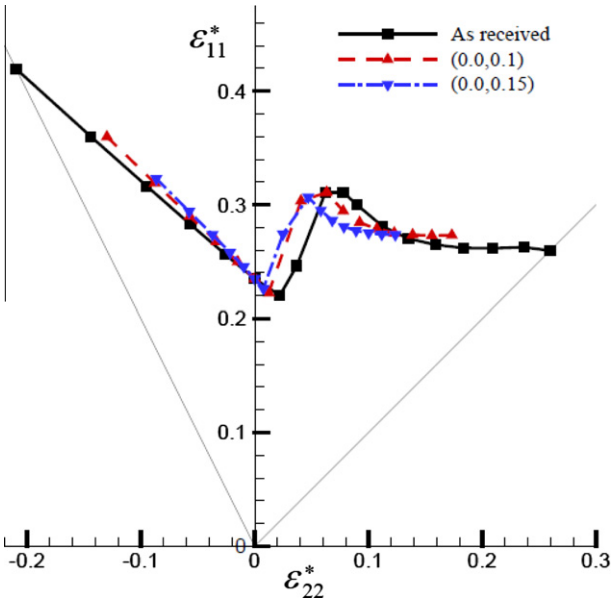

Fig. 17. Predicted FLDs for the reference sheet pre-strained to different levels in in-plane plane strain tension ($\rho = 0$) based on the Affine model.

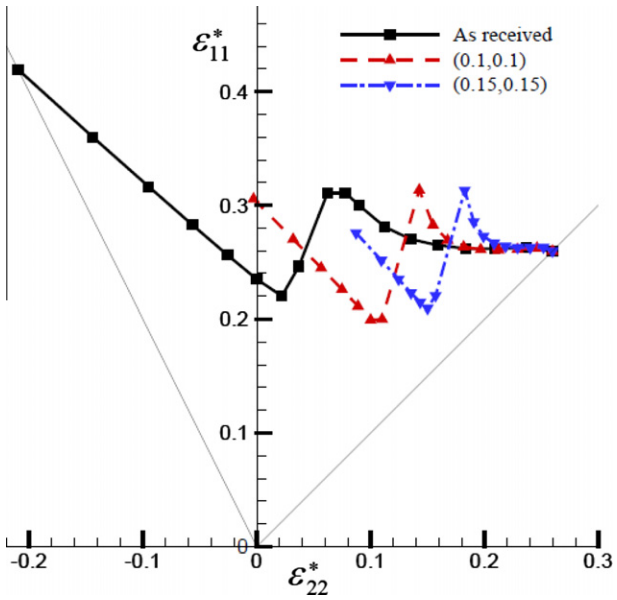

Fig. 18. Predicted FLDs for the reference sheet pre-strained to different levels in equi-biaxial tension ($\rho = 1$) based on the Affine model.

with subsequent in-plane plane strain tension following the equi-biaxial tension pre-strain is predicted to shift to slightly lower major strain and to significantly increase the minor strain. This results in lowering the forming limits for most strain combinations in the region to the right of in-plane plane strain tension.

Figs. 16–18 clearly indicate that the FLD of the HCP sheet is very sensitive to strain path changes. The limit strains could be either raised or lowered depending on the nature of the strain path change. This observation is similar to the general trends of effects of strain path changes on forming limits in steel and aluminum sheets (Laukonis and Ghosh, 1978; Graf and Hosford, 1994).

As mentioned previously, extensive researches on FCC and BCC polycrystalline sheets have confirmed that while the FLD is very sensitive to strain path changes, the FLSD is much less path-dependent (see, e.g. Stoughton, 2000; Wu et al., 2000, 2005). However, the FLSD and its path-dependency have not been studied for HCP polycrystalline sheets. Fig. 19 gives the predicted limit

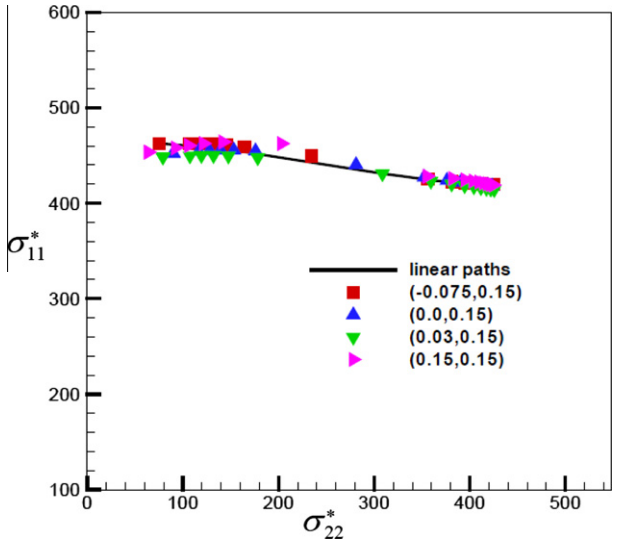

Fig. 19. Predicted limit stresses for the reference sheet pre-strained in various different pre-straining paths indicated by different symbols based on the Affine model.

stresses under proportional (linear) and non-proportional loading histories, shown as different symbols in the figure. For example, the legend "(−0.075,0.15)" indicates that the sheet is pre-strained in strain path $\rho = \frac{-0.075}{0.15} = -0.5$ up to strains $\varepsilon_{22} = -0.075$ and $\varepsilon_{11} = 0.15$. It is noted that in addition to the three pre-strains reported in Figs. 16–19 also includes a case with the legend "(0.03,0.15)", in which the sheet is pre-strained in strain path $\rho = \frac{0.03}{0.15} = 0.2$ up to strains $\varepsilon_{22} = 0.03$ and $\varepsilon_{11} = 0.15$. It is clear that the predicted FLSDs under non-proportional loading histories are close to the FLSD under linear loading. Therefore, the predicted FLSD is not sensitive to strain path changes for magnesium alloy AZ31B sheet.

It is worth mentioning that the effects of strain path changes on the predicted FLDs and FLSDs shown in Figs. 16–19 are based on the Affine model. However, similar results have been obtained by using the Taylor and meff models as well.

5. Conclusions

In this paper, we have calculated FLDs based on the classical Taylor model and the recently developed EVPSC model with various self-consistent schemes, in conjunction with the M–K approach, for magnesium alloy AZ31B sheet. In all the polycrystal plasticity models considered, both slip and twinning contribute to plastic deformations. The material parameters for the various models were first fitted to experimental uniaxial tension and compression curves along the RD and then used to predict FLDs. The effects of initial texture, texture evolution, strain rate-sensitivity, and strain path changes on forming limits have been studied. The numerical results have been found to be in good qualitative agreement with experimental observations. The following conclusions can be drawn:

(1) Formability of HCP sheets can be improved by rotating the basal pole around the TD even without grain refinement.
(2) If values of material parameters in constitutive models are determined by best-fitting the same experimental data, the constitutive models predict similar FLDs for magnesium alloy AZ31B sheet. In other words, the difference in the predicted FLDs between various models is quantitative rather than qualitative.
(3) While the FLD is very sensitive to strain path changes, the FLSD is much less path-dependent. This implies that the FLSD is much more favourable than the FLD in representing forming limits in the numerical simulation of sheet metal forming processes.

Acknowledgement

This research was supported by funding from the NSERC Magnesium Strategic Research Network. More information on the Network can be found at www.MagNET.ubc.ca.

References

Agnew, S.R., Horton, J.A., Lillo, T.M., Brown, D.W., 2004. Enhanced ductility in strongly textured magnesium produced by equal channel angular processing. Scripta Materialia 50, 377–381.
Agnew, S.R., Yoo, M.H., Tomé, C.N., 2001. Application of texture simulation to understanding mechanical behavior of Mg and solid solution alloys containing Li or Y. Acta Materialia 49, 4277–4289.
Arrieux, R., 1995. Determination and use of the forming limit stress diagrams in sheet metal forming. Journal of Materials Processing Technology 53, 47–56.
Arrieux, R., Bedrin, C., Boivin, M., 1982. Determination of an intrinsic forming limit stress diagram for isotropic metal sheets. In: Proceedings of the 12th Biennial Congress IDDRG, pp. 61–71.
Asaro, R.J., Needleman, A., 1985. Texture development and strain hardening in rate dependent polycrystals. Acta Metallurgica Et Materialia 33, 923–953.

Chino, Y., Iwasaki, H., Mabuchi, M., 2007. Stretch formability of AZ31 Mg alloy sheets at different testing temperatures. Materials Science and Engineering A 466, 90–95.
Chino, Y., Sassa, K., Mabuchi, M., 2008. Enhancement of tensile ductility of magnesium alloy produced by torsion extrusion. Scripta Materialia 59, 399–402.
Eshelby, J.D., 1957. The determination of the elastic field of an ellipsoidal inclusion, and related problems. Proceedings of The Royal Society A 241, 376–396.
Graf, A., Hosford, W.F., 1994. The influence of strain-path changes on forming limit diagrams of Al 6111 T4. International Journal of Mechanical Sciences 36, 897–910.
Hecker, S.S., 1975. Formability of aluminum alloy sheet. Journal of Engineering Materials and Technology 97, 66–73.
Hill, R., 1948. A theory of the yielding and plastic flow of anisotropic metals. Proceedings of the Royal Society of London A 193, 281–297.
Hiwatashi, S., Van Bael, A., Van Houtte, P., Teodosiu, C., 1998. Prediction of forming limit strains under strain-path changes: application of an anisotropic model based on texture and dislocation structure. International Journal of Plasticity 14, 647–669.
Hosford, W.A., 1979. On yield loci of anisotropic cubic metals. In: Proceedings of the 7th North American Metalworking Conference, SME, Dearborn, MI, pp. 191–197.
Huang, X.S., Suzuki, K., Watazu, A., Shigematsu, I., Saito, N., 2008. Mechanical properties of Mg–Al–Zn alloy with a tilted basal texture obtained by differential speed rolling. Materials Science and Engineering A 488, 214–220.
Hutchinson, J.W., 1976. Bounds and self-consistent estimates for creep of polycrystalline materials. Proceedings of the Royal Society of London A 348, 101–127.
Hutchinson, J.W., Neale, K.W., 1977. Influence of strain-rate sensitivity on necking under uniaxial tension. Acta Metallurgica 25, 839–846.
Inal, K., Neale, K.W., Aboutajeddine, A., 2005. Forming limit comparisons for FCC and BCC sheets. International Journal of Plasticity 21, 1255–1266.
Inal, K., Wu, P.D., Neale, K.W., 2002a. Instability and localized deformation in polycrystalline solids under plane strain tension. International Journal of Solids and Structures 39, 983–1002.
Inal, K., Wu, P.D., Neale, K.W., 2002b. Finite element analysis of localization deformation in FCC polycrystalline sheets under plane stress tension. International Journal of Solids and Structures 39, 3469–3486.
Jain, A., Agnew, S.R., 2007. Modeling the temperature dependent effect of twinning on the behavior of magnesium alloy AZ31B sheet. Materials Science and Engineering A 462, 29–36.
Kalidindi, S.R., 1998. Incorporation of deformation twinning in crystal plasticity models. Journal of the Mechanics and Physics of Solids 46, 267–290.
Kikuma, T., Nakajima, K., 1971. Effects of the deforming conditions and mechanical properties on the stretch forming of steel sheets. Transactions of the Iron and Steel Institute of Japan 11, 827–839.
Knockaert, R., Chastel, Y., Massoni, E., 2002. Forming limits prediction using rate-independent polycrystalline plasticity. International Journal of Plasticity 18, 231–247.
Kuroda, M., Ikawa, S., 2004. Texture optimization of rolled aluminum alloy sheets using a genetic algorithm. Materials Science and Engineering A 385, 235–244.
Kuroda, M., Tvergaard, V., 2000. Effect of strain path change on limits to ductility of anisotropic metal sheets. International Journal of Mechanical Sciences 42, 867–887.
Laukonis, J.V., Ghosh, A.K., 1978. Effects of strain path changes on the formability of sheet metals. Metallurgical Transactions A 9, 1849–1856.
Lebensohn, R.A., Tomé, C.N., 1993. A self-consistent anisotropic approach for the simulation of plastic-deformation and texture development of polycrystals – application to zirconium alloys. Acta Metallurgica Et Materialia 41, 2611–2624.
Lebensohn, R.A., Tomé, C.N., Castaneda, P.P., 2007. Self-consistent modelling of the mechanical behaviour of viscoplastic polycrystals incorporating intragranular field fluctuations. Philosophical Magazine 87, 4287–4322.
Lévesque, J., Inal, K., Neale, K.W., Mishra, R.K., 2010. Numerical modeling of formability of extruded magnesium alloy tubes. International Journal of Plasticity 26, 65–83.
Marciniak, Z., Kuczynski, K., 1967. Limit strains in the process of stretch-forming sheet metal. International Journal of Mechanical Sciences 9, 609–620.
Molinari, A., Canova, G.R., Ahzi, S., 1987. A self-consistent approach of the large deformation polycrystal viscoplasticity. Acta Metallurgica 35, 2983–2994.
Molinari, A., Tóth, L.S., 1994. Tuning a self-consistent viscoplastic model by finite element results. Part I: Modeling. Acta Metallurgica Et Materialia 42, 2453–2458.
Mukai, T., Yamanoi, M., Watanabe, H., Higashi, K., 2001. Ductility enhancement in AZ31 magnesium alloy by controlling its grain structure. Scripta Materialia 45, 89–94.
Neale, K.W., Chater, E., 1980. Limit strain predictions for strain-rate sensitive anisotropic sheets. International Journal of Mechanical Sciences 22, 563–574.
Neil, C.J., Agnew, S.R., 2009. Crystal plasticity-based forming limit prediction for non-cubic metals: application to Mg alloy AZ31B. International Journal of Plasticity 25, 379–398.
Reed-Hill, R.E., Robertson, W.D., 1957. Deformation of magnesium single crystals by nonbasal Slip. Transactions of the AIME 209, 496–502.
Signorelli, J.W., Bertinetti, M.A., 2009. On the role of constitutive model in the forming limit of FCC sheet metal with cube orientations. International Journal of Mechanical Sciences 51, 473–480.
Signorelli, J.W., Bertinetti, M.A., Turner, P.A., 2009. Predictions of forming limit diagrams using a rate-dependent polycrystal self-consistent plasticity model. International Journal of Plasticity 25, 1–25.
Stoughton, T.B., 2000. A general forming limit criterion for sheet metal forming. International Journal of Mechanical Sciences 42, 1–27.
Stoughton, T.B., Zhu, X., 2004. Review of theoretical models of the strain-based FLD and their relevance to the stress-based FLD. International Journal of Plasticity 20, 1463–1486.
Taylor, G.I., 1938. Plastic strain in metals. Journal of the Institute of Metals 62, 307–324.
Tomé, C.N., Lebensohn, R.A., Kocks, U.F., 1991. A model for texture development dominated by deformation twinning – application to zirconium alloys. Acta Metallurgica Et Materialia 39, 2667–2680.
Tomé, C.N., 1999. Self-consistent polycrystal models: a directional compliance criterion to describe grain interactions. Modelling and Simulation in Materials Science and Engineering 7, 723–738.
Wang, Y.C., Mora, P., 2008. Macroscopic elastic properties of regular lattices. Journal of the Mechanics and Physics of Solids 56, 3459–3474.
Wang, H., Raeisinia, B., Wu, P.D., Agnew, S.R., Tomé, C.N., 2010a. Evaluation of self-consistent polycrystal plasticity models for magnesium alloy AZ31B sheet. International Journal of Solids and Structures 47, 2905–2917.
Wang, H., Wu, P.D., Gharghouri, M.A., 2010b. Effects of basal texture on mechanical behaviour of magnesium alloy AZ31B sheet. Materials Science and Engineering A 527, 3588–3594.
Wang, H., Wu, P.D., Tomé, C.N., Huang, Y., 2010c. A finite strain elastic–viscoplastic self-consistent model for polycrystalline materials. Journal of the Mechanics and Physics of Solids 58, 594–612.
Ward Flynn, P., Mote, J., Dorn, J.E., 1961. On the thermally activated mechanism of prismatic slip in magnesium single crystals. Transactions of the TMS-AIME 221, 1148–1154.
Wu, P.D., Graf, A., Jain, M., MacEwen, S.R., 2000. On alternative representation of forming limits. Key Engineering Materials 177–180, 517–522.
Wu, P.D., Graf, A., MacEwen, S.R., Lloyd, D.J., Jain, M., Neale, K.W., 2005. On forming limit stress diagram analysis. International Journal of Solids and Structures 42, 2225–2241.
Wu, P.D., Jain, M., Savoie, J., MacEwen, S.R., Tugcu, P., Neale, K.W., 2003. Evaluation of anisotropic yield function for aluminum sheets. International Journal of Plasticity 19, 121–138.
Wu, P.D., Lloyd, D.J., Jain, M., Neale, K.W., Huang, Y., 2007. Effects of spatial grain orientation distribution and initial surface topography on sheet metal necking. International Journal of Plasticity 23, 1084–1104.
Wu, P.D., MacEwen, S.R., Lloyd, D.J., Neale, K.W., 2004a. Effect of cube texture on sheet metal formability. Materials Science and Engineering A 364, 182–187.
Wu, P.D., MacEwen, S.R., Lloyd, D.J., Neale, K.W., 2004b. A mesoscopic approach for predicting sheet metal formability. Modelling and Simulation in Materials Science and Engineering 12, 511–527.
Wu, P.D., Neale, K.W., Van der Giessen, E., 1997. On crystal plasticity FLD analysis. Proceedings of the Royal Society of London A 453, 1831–1848.
Wu, P.D., Neale, K.W., Van der Giessen, E., Jain, M., Makinde, A., MacEwen, S.R., 1998. Crystal plasticity forming limit diagram analysis of rolled aluminum sheets. Metallurgical and Materials Transactions 29A, 527–535.
Yoshida, K., Ishizaka, T., Kuroda, M., Ikawa, S., 2007. The effects of texture on formability of aluminum alloy sheets. Acta Materialia 55, 4499–4506.
Zhao, L., Sowerby, R., Sklad, M.P., 1996. A theoretical and experimental investigation of limit strains in sheet metal forming. International Journal of Mechanical Sciences 38, 1307–1317.
Zhou, Y., Neale, K.W., 1995. Predictions of forming limit diagrams using a rate-sensitive crystal plasticity model. International Journal of Mechanical Sciences 37, 1–20.